TRANSIENT SOUND FIELDS FROM IMPACTED PLATES: COMPARISON BETWEEN NUMERICAL SIMULATIONS AND EXPERIMENTS

S. Schedin

Division of Experimental Mechanics, Luleå University of Technology, SE-97187 Luleå, Sweden

AND

C. Lambourge and A. Chaigne

Ecole Nationale Supérieure des Télécommunications, Départment TSI, CNRS URA 820, 46 Rue Barrault, 75634 Paris Cedex 13, France

A comparison between measured and simulated transient acoustic fields generated by a thin rectangular impacted steel plate is reported. The plate vibration is modelled in the time domain using a finite difference scheme of second-order in time and fourth-order in space (2-4 scheme) and the radiated acoustic pressure is obtained by solving numerically the Rayleigh integral equation by using a simple Boundary Element Method (trapezoidal rule). The simulated results are evaluated in the form of the spatial pressure distribution at times short-after the impact excitation. The measurements are performed using an optical method: pulsed two-reference-beam holographic interferometry. Results in the form of 2-D projections of the acoustic pressure field are obtained and compared with the simulations. A high degree of similarity is found between the measured and simulated sound fields.

© 1999 Academic Press

1. INTRODUCTION

Mechanical impacts often give rise to acoustic radiation. Impact noise arises in processes like riveting, forging, stamping and in numerous other hammer-type operations. In addition to the direct sound radiation from the impacted bodies, transmission of impact noise through coupled structures usually occurs. This so called structure-borne sound is of importance, for example, in thin-walled structures in vehicles and machineries subjected to transient excitation. The transient part of such sound fields is of interest in the studies for controlling and reducing noise. The initial behavior of a sound field is also of importance from a perceptual point of view. Differences between tonal qualities or timbres, as interpreted by our hearing, can partly be explained by different transient components of the sound [1]. For example, if the transient part of a tone from

a musical instrument is removed, a listener will in most cases not easily distinguish between different instruments.

Pulsed holographic interferometry is a non-contacting and whole-field optical technique that measures transient events like acoustic waves in air and liquids in a time resolved manner [2–4]. Because of the very short duration (~ 30 ns) of the emitted light from pulsed lasers rapid events such as propagating sound waves are "frozen" at a pulsed holographic recording. A double exposed hologram (comparing a disturbed and an undisturbed state of the air) gives an interference pattern which can be related directly to the spatial distribution of the sound pressure field.

The purpose of this paper is to compare a numerical model for sound radiation from a transiently vibrating plate with measurements. For that reason, an experiment is designed with a cantilever plate impacted by an air-gun lead bullet. The propagating sound field from the plate is recorded at different instants of time shortly after the impact. Results are presented as two-dimensional projections of the sound field showing acoustic waves due to compression and expansion of the air.

For the numerical modelling of transient sound fields, time-domain rather than frequency-domain methods are used. The evolving sound field from an impact excited structure can then be studied in a time-resolved manner in the near field from the start of the excitation. The numerical simulation is based on a finite difference formulation of the flexural wave equation in an isotropic plate excited by a pulse representing the impact of the bullet. A Rayleigh integral equation is used for obtaining the radiated pressure at each time step from the displacement pattern of the plate. The pressure is calculated at a number of spatial points in the near field of the plate and presented as a pattern of acoustic waves. In this way, the simulated results can be compared directly with the optically measured pressure distributions.

2. BASIC EXPERIMENT

A 0·5-g lead bullet of length 5·5 mm (B), with velocity of about 100 m/s, is fired towards a cantilever steel plate (CP); see Figure 1. The impact velocity is calculated from the time difference (about 1 ms) between two signals: one delivered by a trigger laser beam located 10 cm in front of the plate and a second delivered by a strain gauge glued to the plate. Just before the bullet hits the plate the first laser pulse is emitted from the double pulsed ruby laser (RL) giving a recording at the holographic plate (HP) of the undisturbed state of the air surrounding the plate. The second laser pulse (pre-set relative to the first one) is fired a few fractions of a millisecond after the impact, now giving a second recording at the same holographic plate of the disturbed state of the air. A more detailed description of the experimental set-up can be found in reference [2]. The acoustic field is recorded at instants of time shortly after impact, before it has been reflected at the surrounding surfaces. The steel block (SB) behind the cantilever plate is used for reflection of the laser light and is not a part of the acoustic experiment. It is placed
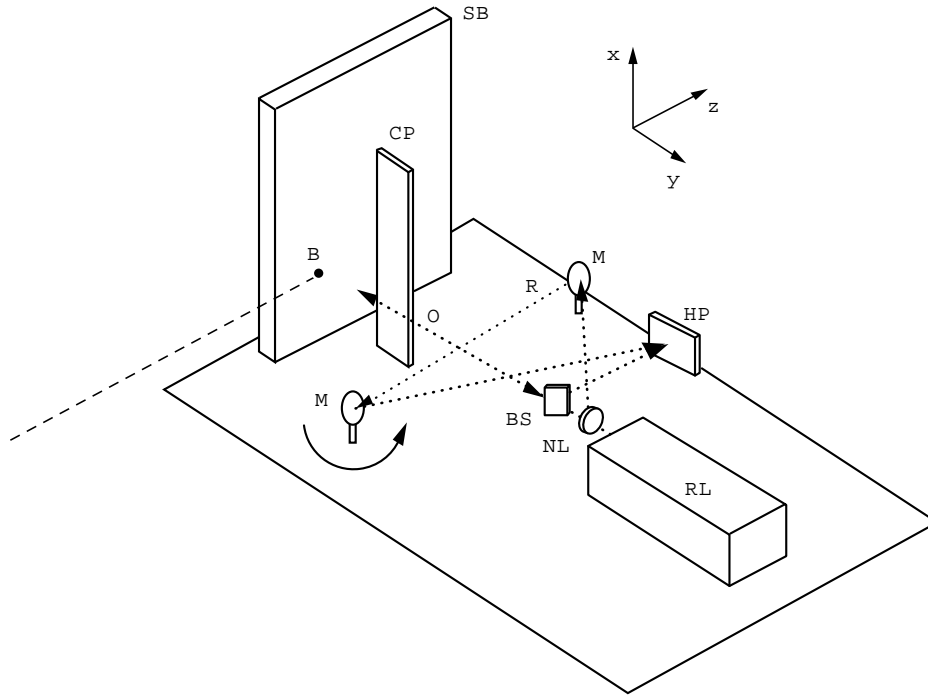
Figure 1. The experimental set-up for pulsed holographic recording. (B) air-gun bullet; (BS) beam splitter; (CP) cantilever plate; (HP) holographic plate; (NL) negative lens; (M) mirrors; (O) object beam; (R) reference beam; (RL) double pulsed ruby laser; (SB) steel block.

at enough distance from the plate to ensure that no reflected acoustic waves will be present in the recordings.

As a result of the acoustic pressure disturbance at the second holographic recording, the index of refraction is changed a small amount giving an optical path difference, ΔL, between the first and second recordings. For small changes of the index of refraction, bending of the light rays is negligible and ΔL can be expressed as [5]

$$\Delta L = \int [n(x, y, z) - n_0] \, \mathrm{d}y, \tag{1}$$

where n_0 is the refractive index representing the undisturbed state of the air and $n(x, y, z)$ is the refractive index distribution along the optical path in the second exposure. The optical path difference appears as interference fringes in the reconstructed hologram. Normally in holographic interferometry, the fringes do not give information on the sign of ΔL. This ambiguity is resolved in this experiment by using the two-reference-beam holographic technique, as described in reference [2]. The interference fringes can be related directly to the change in density along the optical path, because there exists a relation between refractive index and density, the Gladstone–Dale equation; see reference [5]. Further, the pressure can be derived from the density by thermodynamic relations. Thus,

two-dimensional projections (pressure maps) of the sound pressure field are obtained from the holographic measurements.

3. NUMERICAL SIMULATION OF THE TRANSIENT SOUND FIELD

3.1. THE PLATE VIBRATION MODEL

It is assumed that the transverse displacement $W(x, y, t)$ of the thin undamped isotropic rectangular steel plate of thickness h and density ρ is governed by the classical system of equations [6]

$$\left\{ \begin{bmatrix} M_x \\ M_y \\ M_{xy} \end{bmatrix} = -D \begin{bmatrix} 1 & v & 0 \\ v & 1 & 0 \\ 0 & 0 & 1-v \end{bmatrix} \begin{bmatrix} \dfrac{\partial^2 W}{\partial x^2} \\ \dfrac{\partial^2 W}{\partial y^2} \\ \dfrac{\partial^2 W}{\partial x\, \partial y} \end{bmatrix} \\ \rho h \dfrac{\partial^2 W}{\partial t^2} = \dfrac{\partial^2 M_x}{\partial x^2} + \dfrac{\partial^2 M_y}{\partial y^2} + 2 \dfrac{\partial^2 M_{xy}}{\partial x\, \partial y} + q(x, y, t) \right\}, \tag{2}$$

where M_x, M_y and M_{xy} are the moments per unit length, $D = Eh^3/12(1 - v^2)$ is the bending stiffness of the plate, E is the Young's modulus and v is the Poisson's ratio. The plate, initially at rest, is set into vibration through the loading $q(x, y, t)$ which represents the impact of the lead bullet. The plate is clamped at the edge along $x = 0$ and free at the three other edges. Therefore, the boundary conditions are

$$W = 0 \quad \text{and} \quad \partial W/\partial x = 0 \quad \text{for} \quad x = 0, \tag{3}$$

$$M_x = 0 \quad \text{and} \quad \partial M_x/\partial x + 2\, \partial M_{xy}/\partial y = 0 \quad \text{for} \quad x = l_x, \tag{4}$$

$$M_y = 0 \quad \text{and} \quad \partial M_y/\partial y + 2\, \partial M_{xy}/\partial x = 0 \quad \text{for} \quad y = 0 \quad \text{and} \quad y = l_y. \tag{5}$$

It is well-known that combining equations (2) yields the equation

$$\rho h\, \partial^2 W/\partial t^2 = -DV^4 W + q(x, y, t), \tag{6}$$

where V^4 is the biharmonic operator. Although equation (6) may appear simpler in the form than the system of equations (2), it is appropriate here to deal with the latter system for the two following reasons. Firstly, it is necessary to know explicitly the expressions for the moments M_x, M_y and M_{xy} in order to calculate the free boundary conditions in equations (4) and (5). Secondly, it turns out that the numerical algorithm is much faster (about a factor of 10) for a system of equations involving second-order partial derivatives only than for a single equation involving fourth-order partial derivatives, such as equation (6).

In what follows, the coupling of the plate with the surrounding fluid is neglected. One argument for justifying this assumption is to calculate the non-dimensional

intrinsic fluid-loading parameter ε at the critical frequency of the plate (see, for example, reference [7]). This parameter is defined as

$$\varepsilon = \rho_a c_a / \rho h \omega_c, \tag{7}$$

where ρ_a is the air density, c_a is the speed of sound in air and ω_c is the circular critical frequency given by

$$\omega_c = 2\pi f_c = \sqrt{\rho h c_a^4 / D}. \tag{8}$$

The condition of negligible coupling is $\varepsilon \ll 1$. In the present case, the critical frequency f_c of the plate is equal to 11 kHz, which leads to $\varepsilon = 7 \cdot 0 \times 10^{-4}$. The critical frequency and the fluid-loading parameter are calculated with the following constants: $\rho_a = 1 \cdot 29$ kg/m^3, $c_a = 340$ m/s, $\rho = 7850$ kg/m^3, $h = 1$ mm, $v = 0 \cdot 3$, $E = 210$ GPa.

3.2. THE FINITE DIFFERENCE FORMULATION

The time domain numerical simulation of the vibrating plate is conducted by using an explicit finite difference scheme of second-order in time and fourth-order in space (a so-called 2-4 scheme) which offers a good compromise between stability conditions, accuracy and computational costs. In order to achieve this, the partial derivatives in the system of equations (2) are approximated by centered finite differences. Thus, the continuous displacement $W(x, y, t)$ is computed on a spatial grid with step sizes $(\Delta x, \Delta y)$ and at discrete instants of time with step size Δt. In what follows, the discrete displacement of the plate is written as

$$W_{l,m}^n \triangleq W(l\Delta x, m\Delta y, n\Delta t), \tag{9}$$

where l, m, and n are integer numbers. The symbol $\triangleq$ means equal by definition. The following finite difference approximations of the partial derivatives involve centered operators for which two different notations are used, depending on whether the approximations are calculated at the grid points themselves or at the centers of the segments between the grid points. For example, a second-order approximation of the first spatial derivative of the displacement W with respect to x at discrete position $(l + 1/2)\Delta x$ is written with the symbolic operator

$$(D_x^{(2)} W)_{l+1/2,m}^n \triangleq \frac{W_{l+1,m}^n - W_{l,m}^n}{\Delta x}. \tag{10}$$

Similarly, a second-order approximation of the first spatial derivative of the displacement W with respect to x at discrete position $l\Delta x$ is written with the symbolic operator

$$(\tilde{D}_x^{(2)} W)_{l,m}^n \triangleq \frac{W_{l+1/2,m}^n - W_{l-1/2,m}^n}{\Delta x}. \tag{11}$$

In order to obtain a fourth-order approximation in space, the second partial derivatives of W with respect to x and y, respectively, are approximated by the operators

$$(D_{xx}^{(4)}W)_{l,m}^n \triangleq \frac{1}{12\Delta x^2}[-(W_{l+2,m}^n + W_{l-2,m}^n) + 16(W_{l+1,m}^n + W_{l-1,m}^n) - 30W_{l,m}^n],$$

(12)

and

$$(D_{yy}^{(4)}W)_{l,m}^n \triangleq \frac{1}{12\Delta y^2}[-(W_{l,m+2}^n + W_{l,m-2}^n) + 16(W_{l,m+1}^n + W_{l,m-1}^n) - 30W_{l,m}^n].$$

(13)

Similar operators are used for approximating the second-order partial derivatives of the moments M_x and M_y with respect to x and y.

The cross partial derivative of the form $\partial^2 W/\partial x\,\partial y$ is approximated by the operator

$$
\begin{aligned}
(D_{xy}^{(4)}W)_{l+1/2,m+1/2}^n \triangleq \frac{1}{24^2\Delta x\Delta y}[&(W_{l-1,m-1}^n + W_{l+2,m+2}^n - W_{l-1,m+2}^n - W_{l+1,m-1}^n), \\
&+ 27(W_{l-1,m+1}^n + W_{l,m+2}^n + W_{l+1,m-1}^n + W_{l+2,m}^n) \\
&- 27(W_{l-1,m}^n + W_{l,m-1}^n + W_{l+1,m+2}^n + W_{l+2,m+1}^n) \\
&+ 27^2(W_{l,m}^n + W_{l+1,m+1}^n - W_{l+1,m}^n - W_{l,m+1}^n)].
\end{aligned}
$$

(14)

Finally, the cross partial derivative of the form $\partial^2 M_{xy}/\partial x\,\partial y$ is approximated by the operator:

$$
\begin{aligned}
(\tilde{D}_{xy}^{(4)}M_{xy})_{l,m}^n \triangleq \frac{1}{24^2\Delta x\Delta y}[&((M_{xy})_{l-3/2,m-3/2}^n + (M_{xy})_{l+3/2,m+3/2}^n - (M_{xy})_{l+3/2,m-3/2}^n \\
&- (M_{xy})_{l-3/2,m+3/2}^n) + 27((M_{xy})_{l-3/2,m+1/2}^n + (M_{xy})_{l-1/2,m+3/2}^n \\
&+ (M_{xy})_{l+1/2,m-3/2}^n + (M_{xy})_{l+3/2,m-1/2}^n) - 27((M_{xy})_{l-3/2,m-1/2}^n \\
&+ (M_{xy})_{l-1/2,m-3/2}^n + (M_{xy})_{l+1/2,m+3/2}^n + (M_{xy})_{l+3/2,m+1/2}^n) \\
&+ 27^2((M_{xy})_{l-1/2,m-1/2}^n + (M_{xy})_{l+1/2,m+1/2}^n - (M_{xy})_{l+1/2,m-1/2}^n \\
&- (M_{xy})_{l-1/2,m+1/2}^n)].
\end{aligned}
$$

(15)

With the help of the finite difference operators defined in equations (12)–(15) and approximating further the time derivative by a second-order finite difference scheme, the system of equations (2) becomes

$$
\begin{pmatrix} (M_x)_{l,m}^n \\ (M_y)_{l,m}^n \\ (M_{xy})_{l+1/2,m+1/2}^n \end{pmatrix} = -D\begin{pmatrix} 1 & v & 0 \\ v & 1 & 0 \\ 0 & 0 & 1-v \end{pmatrix}\begin{pmatrix} (D_{xx}^{(4)}W)_{l,m}^n \\ (D_{yy}^{(4)}W)_{l,m}^n \\ (D_{xy}^{(4)}W)_{l+1/2,m+1/2}^n \end{pmatrix},
$$

$$
\begin{aligned}
W_{l,m}^{n+1} = 2W_{l,m}^n - W_{l,m}^{n-1} - \frac{\Delta t^2 D}{\rho h}&[(D_{xx}^{(4)}M_x)_{l,m}^n + (D_{yy}^{(4)}M_y)_{l,m}^n \\
&+ 2(\tilde{D}_{xy}^{(4)}M_{xy})_{l,m}^n + q_{l,m}^n].
\end{aligned}
$$

(16)

With this scheme, the truncation error in the approximations of the spatial derivatives is of second-order in time and fourth-order in space, which is consistent with the order of the derivatives. A generalization of equations (16) can be made for viscoelastic orthotropic plates [8].

The numerical formulation of the boundary conditions expressed in equations (3)–(5) are obtained by means of the image method. The spatial derivatives are approximated by second-order operators, since it is known that fourth-order approximations leads here to an unconditionally unstable scheme, due to the high number of fictitious points situated outside the plate domain [9]. It has been checked, however, that this second-order approximation of the boundary conditions does not significantly alter the accuracy of the propagation scheme.

3.3. MAIN PROPERTIES OF THE NUMERICAL SCHEME

A rectangular mesh is used for the spatial discretization. Equal step sizes are selected in the x and y directions for isotropy reasons. The value of the spatial step $\Delta x = \Delta y$ is determined in order to ensure the stability of the explicit 2-4 scheme, and to guarantee that the relative dispersion error in phase velocity is smaller than 1% in the audible range.

The stability of the numerical scheme (16) was analyzed with the help of the Fourier method [10]. This leads to the stability condition

$$\Delta x^2 \geqslant \Delta x_{min}^2 = 2\Delta t \sqrt{\frac{2D}{\rho h}} \sqrt{\left(\frac{4}{3}\right)^2 (1 + v) + \left(\frac{7}{6}\right)^4 (1 - v)}. \tag{17}$$

In comparison, the stability condition for a standard centered finite difference scheme of second-order in time and space (2-2 scheme) is written as

$$\Delta x^2 \geqslant \Delta x_{min}^2 = 4\Delta t \sqrt{D/\rho h}. \tag{18}$$

For a steel plate with $v = 0.3$ this means in practice that, for a given time step, the minimum spatial step for the 2-4 scheme must be about 1·16 times higher than for the 2-2 scheme.

The accuracy of the numerical scheme is evaluated in terms of its dispersion properties. The general method consists of comparing the continuous phase velocity of a wave with frequency ω travelling in the plate after the impact with the numerical phase velocity derived from the finite difference scheme [10]. From the continuous plate equation (6) one has

$$\omega = k^2 \sqrt{D/\rho h}, \tag{19}$$

where $k = \sqrt{k_x^2 + k_y^2}$ is the wavenumber. The angle $\theta = \arctan(k_y/k_x)$ corresponds to the direction of propagation of the travelling wave in the plate.

For a given wavenumber k, the frequency ω in equation (19) has to be compared with the numerical frequency ω_{num} derived from the system of equations (16). The accuracy of the numerical scheme depends on the propagation angle θ. However, it can be shown (see reference [9]) that the less favorable results are obtained in

the limiting cases $\theta = 0$ or $\theta = \pi/2$: i.e., for waves propagating parallel to the axes. With $\Delta y = \Delta x = \Delta x_{min}$ and a given Δt, one has, for the 2-4 scheme,

$$\omega_{num}(\omega) = \frac{2}{\Delta t} \arcsin \left[\frac{\sin^2 a\sqrt{\omega \Delta t} + \frac{1}{3} \sin^4 a\sqrt{\omega \Delta t}}{2a^2} \right], \tag{20}$$

with

$$a = \left[\left(\frac{4}{3} \right)^2 \frac{(1+v)}{2} + \left(\frac{7}{6} \right)^4 \frac{(1-v)}{2} \right]^{1/4}.$$

The relative error in phase velocity is given by

$$e(\omega) = (\omega - \omega_{num})/\omega. \tag{21}$$

In the present simulations, a time step of 1·3 μs (sampling frequency 768 kHz) has been selected. This yields, for example, a relative error in phase velocity less than 0·7% in the audible range: i.e., for frequencies less than 20 kHz. With this time step, the stability condition expressed in equation (17) yields a spatial step equal to 3·3 mm. At a frequency of 20 kHz, the flexural wavelength is equal to 22 mm. As a consequence the minimum number of points per wavelength N_λ is equal to 6·7 in the audible range. This number becomes equal to 10 at 10 kHz, and equal to 30 at 1 kHz. This grid density is of the same order of magnitude as the one used by Frendi *et al.* in a similar problem [11]. In the present simulations, a sampling frequency reduced by a factor of two (384 kHz) was also tested. However, imperfections appeared in the result images in this case, as a result of the undersampling. Therefore, the higher sampling frequency was selected.

In comparison, the corresponding 2-2 scheme with numerical frequency equal to

$$\omega_{num} = \frac{2}{\Delta t} \arcsin \left[\frac{\sin^2 \sqrt{\omega \Delta t}}{2} \right] \tag{22}$$

would have led to a relative error in phase velocity less than 5·2%.

In conclusion, the explicit 2-4 scheme needs about two times more operations than the 2-2 scheme, but it shows better global properties since its accuracy is improved by a factor of seven in the audio range.

3.4. MODELLING OF THE IMPACT FORCE

Since one does not know exactly the characteristics of the force transmitted from the lead bullet to the plate in the experiments, two additional experiments are performed.

In the first experiment, the impact process was investigated by recording the event by using a high-speed camera (Ultranac image-converter camera) in order to obtain a realistic order of magnitude for the impact duration. Figure 2 shows a sequence of frames of the event. The lower left frame is the first exposure, captured just at the start of contact. In the following 6–7 frames, i.e. during
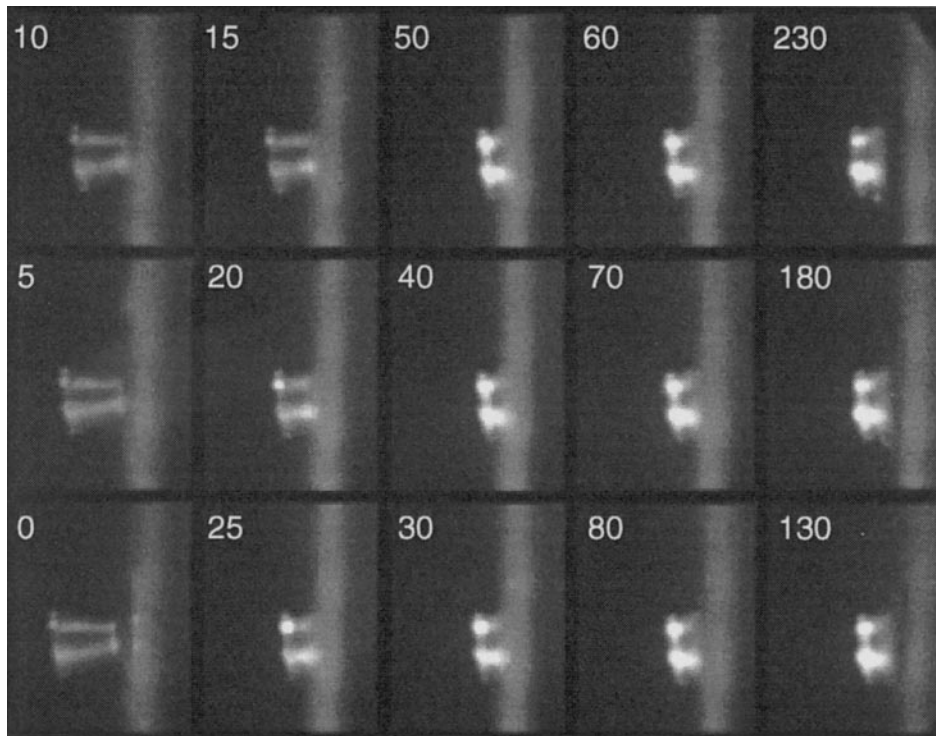
Figure 2. The impact of a lead bullet on a steel plate recorded by a high-speed camera. The time in μs is indicated in the upper left part of each frame.

30–40 μs, the bullet deforms in a plastic way. After 40 μs, it is still in contact but it does not seem to deform any longer. Finally, at 130 μs the bullet is no longer in contact. This suggests that the energy is transferred to the plate mainly during the time the bullet deforms, that is, during the first 30–40 μs after the start of contact. This time is used as an estimate for the duration of impact force in the numerical simulations.

The shape of the force in the simulations is modelled as a sine-wave (Hanning window) where the time derivatives are zero at the beginning and at the end of the force curve. Such a curve is shown in Figure 3. This choice of shape together with a duration of the force of about $t_{max} = 35$ μs was shown to give pressure fields in good agreement with the measured results.

However, since the impact of the lead bullet involved plastic deformation of the material, the real shape of the force will most probably deviate from an ideal symmetric sine wave. A second experiment, in which a piece of lead was impacted by a hammer tip with a mounted force transducer, supported this assumption. The ratio between the rise time of the force and the total duration time turned out to be very repetitive. A series of 20 impacts, all with plastic indentation on the piece of lead and with different magnitudes of the maximum force, gave ratios between rise time and total duration time within the interval 0·64–0·75, with an average of 0·70. An example of the force versus time obtained in this experiment is shown in Figure 4. Although direct conclusions of the behavior of the force in the case

of the lead bullet against the plate cannot be drawn from this experiment, which has been conducted at a much lower impact velocity (less than 5 m/s), one has a clear indication that the force most likely has an asymmetric shape due to plastic deformation. Consequently, it exhibits more energy in the high frequency range than a force of symmetric shape for the same duration (compare the force spectra in Figures 3 and 4). This high-frequency content may be compensated by various causes of damping in the experiments, which explains why the simulations (which include no damping and a symmetric force) are in good agreement with the experiments. In reference [12] further discussions of impacts involving plastic indentations can be found.
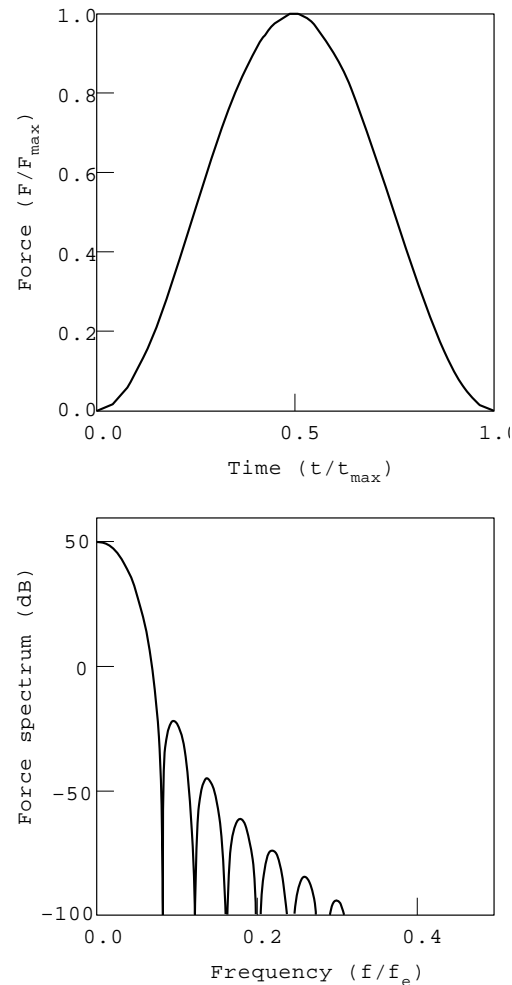
Figure 3. Upper part: sine-wave shape (Hanning window) of the force versus time used in the simulations. Lower part: frequency spectrum of the sine-wave shaped force. f_e is the sampling frequency.
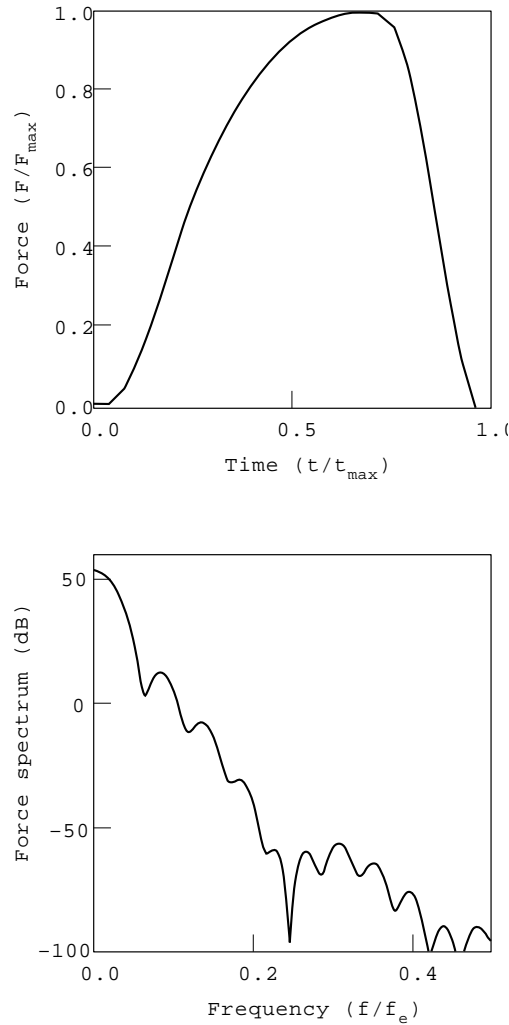
Figure 4. Upper part: force versus time in an impact experiment with an instrumented hammer tip against a piece of lead. Lower part: frequency spectrum of the measured force. f_e is the sampling frequency.

3.5. CALCULATION OF SPATIAL PRESSURE FIELDS

The goal is to visualize the simulated results as the spatial distribution of the pressure field in the same form as the experimental pressure maps. This allows direct comparisons between numerical and experimental results. Thus, the pressure is calculated at a large number of spatial points at one specific time instant shortly after the start of excitation. Figure 5 shows the plate and an example of a plane perpendicular to the plate (in the xy-direction) with points where the pressure is evaluated. For each point, $\mathbf{r}$, in the plane the pressure is calculated by using the Rayleigh integral. It can be written as

$$p(\mathbf{r}, t) = -\frac{\rho_a}{2\pi} \int_{(S)} \frac{1}{|\mathbf{r} - \mathbf{r}_0|} \frac{\partial^2}{\partial t^2} W\left(\mathbf{r}_0, t - \frac{|\mathbf{r} - \mathbf{r}_0|}{c_a}\right) dS, \tag{23}$$

where $|\mathbf{r} - \mathbf{r}_0|$ is the distance from one point in the plane to one point at the plate surface.

Equation (23) is put into a numerical form by using a standard trapezoidal rule, a particular simple form of the Boundary Element Method. This yields, for a rectangular plate of length l_x and width l_y,

$$p(\mathbf{r}, t) = -\frac{\rho_a}{2\pi} \sum_{l=0}^{N_x-1} \sum_{m=0}^{N_y-1} \frac{\Delta x \Delta y}{4} \frac{\partial^2}{\partial t^2} \left(\frac{W_{l,m}(t - R_{l,m}/c_a)}{R_{l,m}} \right.$$

$$+ \frac{W_{l+1,m}(t - R_{l+1,m}/c_a)}{R_{l+1,m}}$$

$$\left. + \frac{W_{l,m+1}(t - R_{l,m+1}/c)}{R_{l,m+1}} + \frac{W_{l+1,m+1}(t - R_{l+1,m+1}/c)}{R_{l+1,m+1}} \right), \qquad (24)$$

where $N_x = l_x/\Delta x$ and $N_y = l_y/\Delta y$. $R_{l,m}$ is the distance between the observation point ($\mathbf{r}$) and the grid point of co-ordinates $l\Delta x$, $m\Delta y$ on the plate.
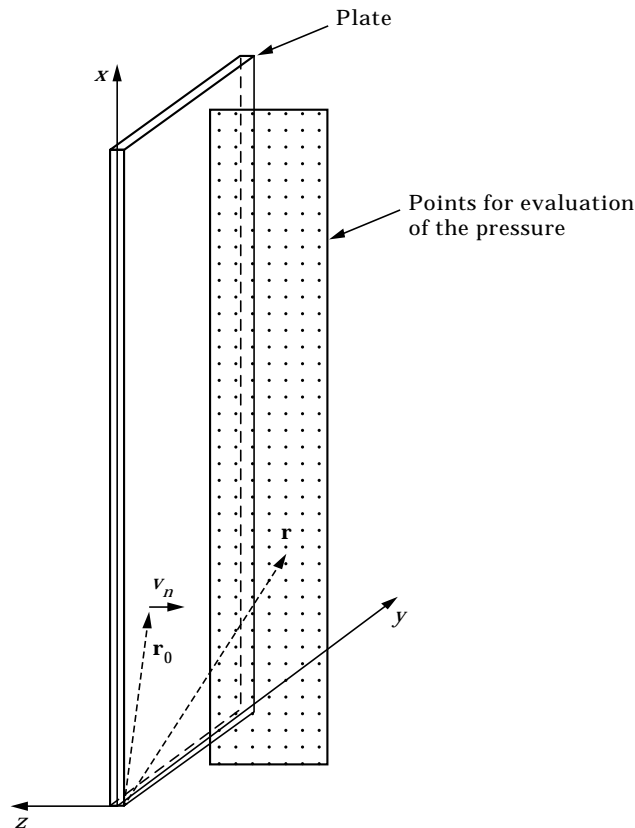

Figure 5. Geometry of the plate and a grid containing points for evaluation of the sound pressure. The plate is clamped at $x = 0$.

The second-order partial derivative versus time in equation (24) can be approximated here by any order finite difference scheme, depending on the desired accuracy. In other words, no coherence is needed with space discretization since there are no spatial derivatives of the displacement involved here. In order to keep the explicit character of the scheme, a backward difference has been selected. A fourth-order approximation of the acceleration, for example, is written as

$$\frac{\partial^2 W_{l,m}}{\partial t^2} = \sum_{i=0}^{6} C_i W_{l,m}^{n-i} + O(\Delta t^4), \qquad (25)$$

with

$$C_0 = 84\,539/24\,480\Delta t^2 \quad C_1 = -3861/340\Delta t^2 \quad C_2 = 8103/544\Delta t^2$$

$$C_3 = -6175/612\Delta t^2 \quad C_4 = 117/32\Delta t^2 \quad C_5 = -48/85\Delta t^2 \quad C_6 = 137/24\,480\Delta t^2.$$

The main limitation of the pressure model follows from the use of the Rayleigh integral which amounts to assuming that the plate is baffled although it is obviously not the case in the experiments. However this method yields good results in the present situation since most of the observations are limited to the very first instants of time after the impact: i.e., before the waves reach the edges of the plate. It will be shown in the next section to what extent the "baffled" assumption affects the agreement between measurements and simulations.

For an appropriate comparison with measured results, a two-dimensional projection of the sound field must be produced. First, the pressure distribution is calculated in a number of planes. These planes are located, for example, across the width of the plate (along the y-direction in Figure 5). Then, an integration (summation) of the pressure values over y is performed. This give a two-dimensional projection which can directly be compared with the optically measured results.

4. RESULTS

Figures 6(a) and 7(a) show simulated pressure distributions outside the steel plate in the xz-plane, see Figure 5, at two successive instants of time shortly after the start of impact (140 and 185 μs, respectively). The dimensions of the plate are $300 \times 30 \times 1$ mm. The edge of the plate is indicated in the middle of the figures as a black vertical line. Bright and dark regions indicate positive and negative sound pressure, respectively. The images show the result of summation of the pressure in 25 planes along the y-direction in Figure 5. A spatial step of 1 mm is chosen between the points in one plane and a step of 4 mm between each plane.

Measured pressure distributions at the same times as above are shown in Figures 6(b) and 7(b). In both images, up and down the plate, trace-matched acoustic waves with alternating positive and negative pressures are seen. These are generated by the flexural bending waves in the plate travelling faster than the speed of sound in air. Further away from the impacting point, the wavelength and the radiating angle between the waves and the plate become smaller. This feature,
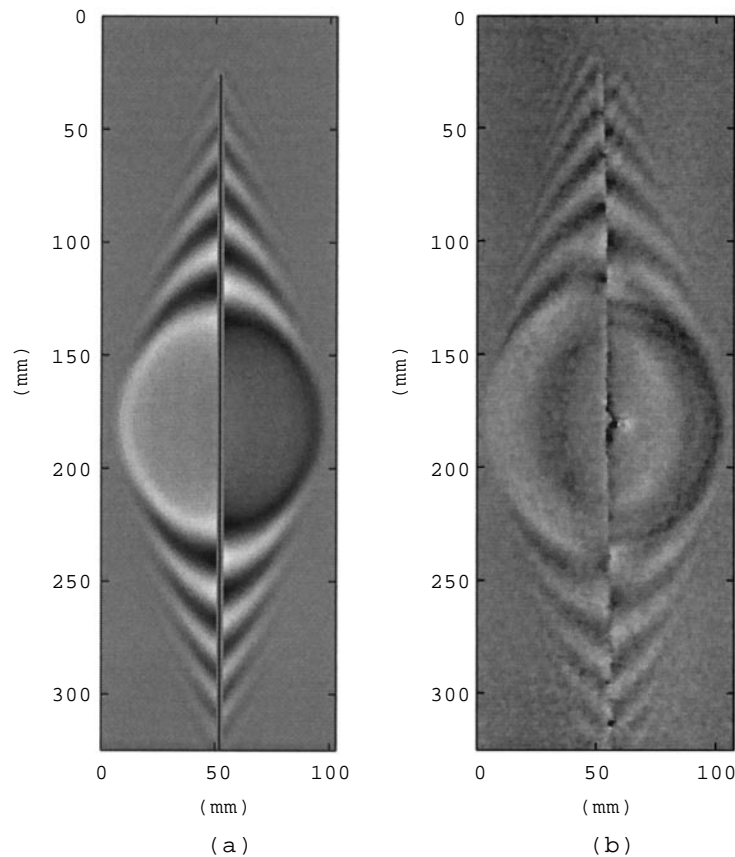
Figure 6. Sound pressure distributions (in the x–z plane) at 140 µs after impact start. (a) Simulated; (b) measured.

which is due to the dispersive character of the travelling flexural waves in the plate, is well-captured in the simulated results.

Above the upper edge of the plate in the fields at 185 µs, differences between Figures 7(a) and (b) can be observed. These differences can be explained by restrictions in the numerical model (baffled model) implying that there is no interaction of sound waves between the left- and right-hand sides of the plate, which is obviously not the case in our experiments which have been conducted with an unbaffled plate. Therefore, outside the edge of the plate in directions to its plane comparisons cannot be made.

Around the impacting point, at the center in Figures 6 and 7, the direct wavefront (moving with the speed of sound in air) is seen. Comparing the (a) and (b) figures shows that the outer parts of this wave seem to agree quite well. However, the lead bullet impact is a complex process which involves several non-linear effects which influence the direct wave and the region close to the impacting point. The high velocity of the lead bullet in the experiments leads to a large deformation of the plate at the impacting point. Also, the plastic deformation of the bullet produces thermal energy. At short times after impact, the heat generated has not dissipated leading to a local increase in the temperature
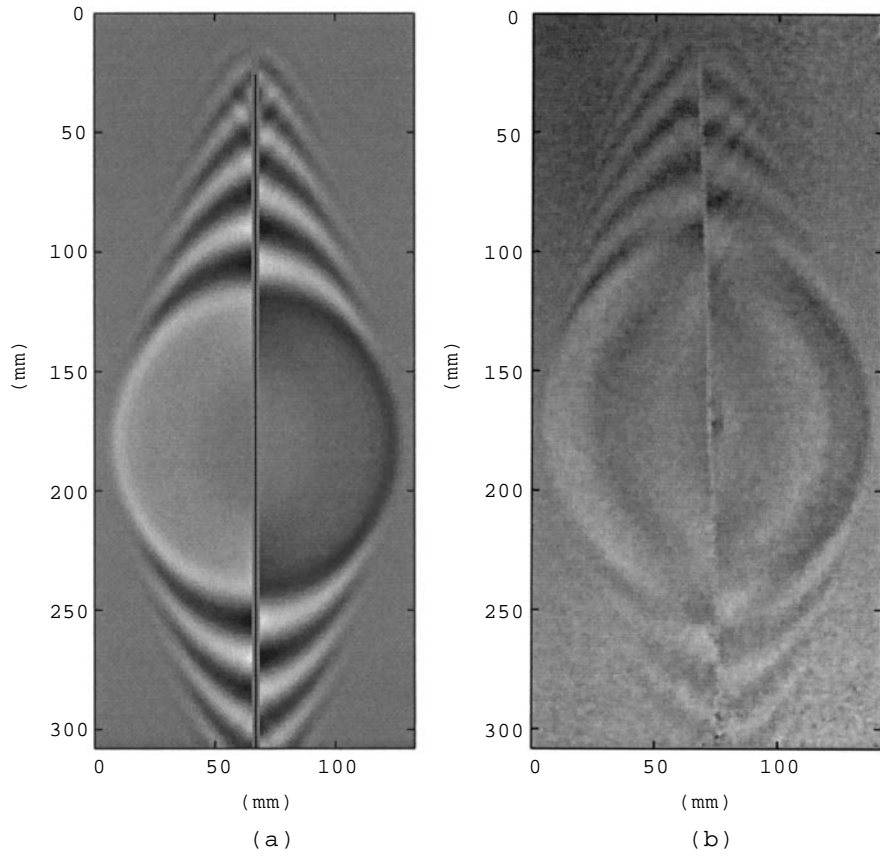
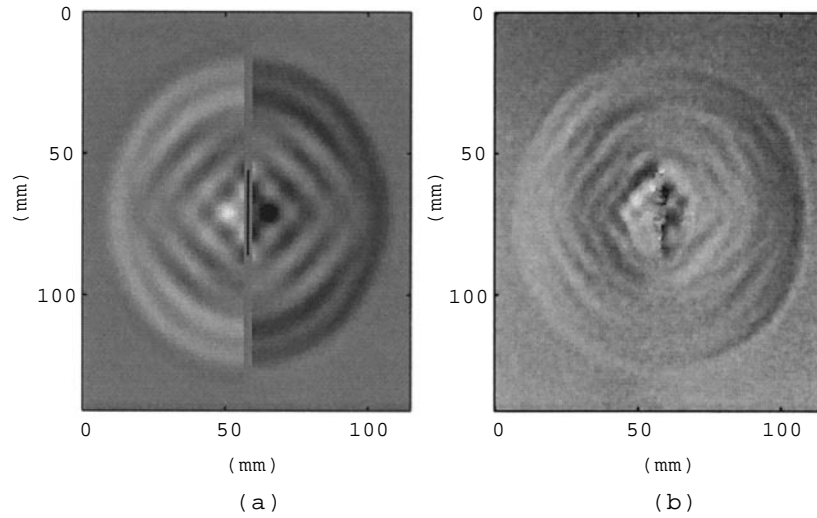Figure 7. Sound pressure distributions (in the x–z plane) at 185 μs after impact start. (a) Simulated; (b) measured.

Figure 8. Sound pressure distributions (in the x–z plane) at 155 μs after impact start. (a) Simulated; (b) measured.

at the impacting point. Non-linear effects like these are not taken into account in the numerical model. Therefore, detail comparisons in this region of the sound field must be performed with care.

The sound field is also studied in the *yz*-plane, viewed along the *x*-axis in Figure 5. Figure 8(a) shows a simulated projection of the field at 155 µs after impact. The upper edge of the plate is indicated by the black line along the boundary between the left and right halves of the field. In this case the dimensions of the plate are 190 × 30 × 1 mm, and the excitation is applied 15 mm from the upper edge. This projection is a result of summation of the pressure field at 46 slices (*yz*-planes) in the *x*-direction, from 35 mm above down to 120 mm below the excitation point. A step of 4 mm is used between each slice. Note that the pressure magnitude seems to be stronger in directions about 45 degrees from the plate than in directions perpendicular and parallel to the plate. The same observation can be made in the measured projection, shown in Figure 8(b). This projection is obtained with the same experimental set-up as shown in Figure 1 but with an additional mirror placed above the plate. Also, similarities between the wave pattern close to the plate can be found. However, comparisons cannot be performed right outside the edges of the plate. In these regions the numerical model is not valid. As mentioned above, there is no interaction between sound
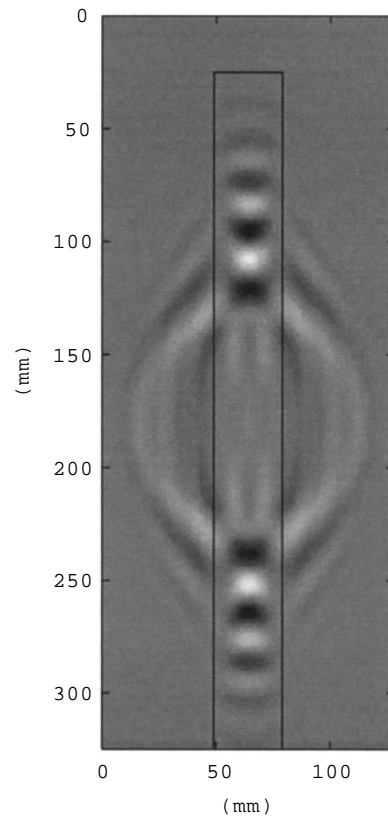

Figure 9. Simulated pressure distribution (in the *x–z* plane) at 140 µs after impact start.

waves from the left and right sides of the plate. That is the reason for the sharp boundary separating the left and right halves of the simulated field in Figure 8(a).

Figure 9 shows a simulated pressure distribution in the xy-plane (see Figure 5), at 5 mm in front of the plate of dimensions $300 \times 30 \times 1$ mm. The contour of the plate is indicated in the image. Note that this distribution corresponds to the pressure in a single plane and not integrated values as in Figures 6(a)–8(a). The trace-matched sound waves are clearly seen in Figure 9 as the small rectangular shaped zones in the upper and lower part of the image with alternating positive and negative pressure. The magnitude of these waves is strong. Also, they are quite constant across the width of the plate. The radiation from the bending waves in this case of a rather narrow plate is mainly two-dimensional. However, this simulation also reveals sound waves propagating in other directions. They can be explained by flexural motion across the width of the plate.

In an additional experiment, the sound pressure was measured by a small condenser microphone, (linear up to 100 kHz), at one particular point outside the upper part of the cantilever plate. The location of this point is in the (x, y, z)-directions (255, 15, 10) mm (see Figure 5). The reason for this choice is to be able to register the radiation of trace-matched waves before the direct sound wave front has reached the microphone (about 300 µs after impact start). Also, having the microphone outside the half-width (middle) of the plate should give a good recording of the trace-matched waves since their variation is strong there, as concluded from the simulated result in Figure 9. A comparative simulation is performed in which the pressure is computed as a function of time at this particular
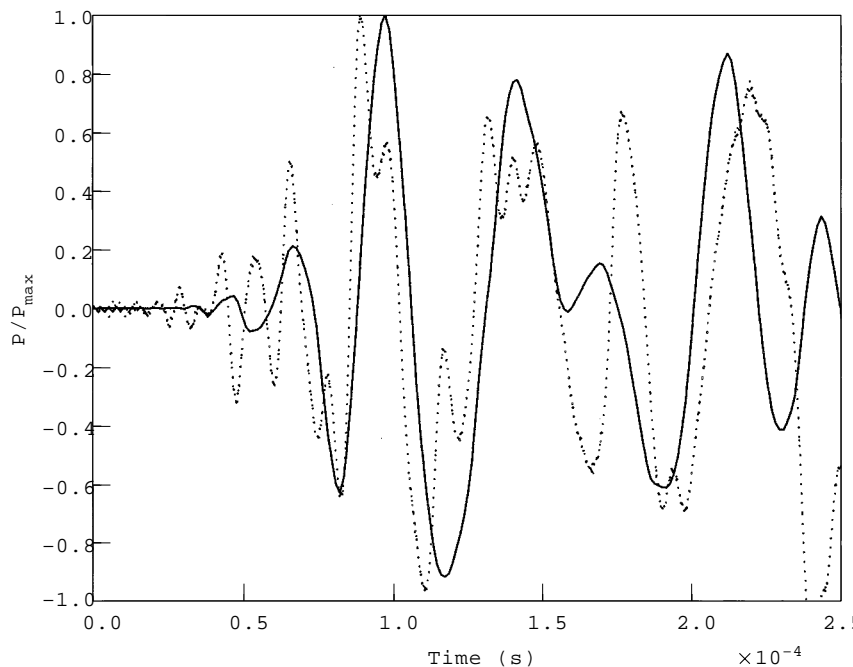

Figure 10. Time histories of the pressure variation at a single point located at (255, 15, 10) mm in the (x, y, z)-directions. Solid curve, simulated pressure; dotted curve, measured pressure.

point. In Figure 10, time histories of the calculated (solid curve) and the measured sound pressure (dotted curve) are shown. A more rapid variation in the measured pressure can be noticed, especially in the beginning. This difference can be explained by higher frequency components in the excitation by the lead bullet in the experiment than in the numerical simulation. However, the large scale variations are quite similar.

5. CONCLUSION

Comparisons between time domain simulations and optically measured transient sound fields radiating from an impacted plate have been performed. Pulsed two-reference beam holographic interferometry was employed for the measurements. The simulations are based on the Kirchhoff plate equation which is solved numerically by an explicit finite difference scheme of second-order in time and fourth-order in space. It has been checked that the Mindlin plate model would not improve significantly the results in the audio range, because of the small thickness of the plate. The sound pressure field due to radiation of the vibrating plate is derived from the transverse displacement of the plate by solving the Rayleigh integral equation (baffled model).

A high degree of similarity is observed between the simulated and measured sound wave patterns within the regions where the baffled model is valid. Sound waves produced by high speed bending waves in the plate are well-reproduced in the simulation. Large deformations of the plate occur in the experiments at the impact point which are not taken into account in the linear model used in the simulations. Despite this fact the overall agreement is quite good in this region, although detailed comparisons must be done with care.

In an additional experiment and simulation, the sound pressure versus time at one point were compared. The large scale variations of the transient part of the sound, produced by bending waves in the plate, agree well. At this stage, it could be remarked that time histories with pointwise information are more difficult to interpret than a spatial pressure map which gives a physical full-field picture of the phenomenon.

The numerical model used is found to be suitable for modelling transient acoustic fields radiated by plates into a light medium like air, in which the effect of fluid-loading is small. It allows a full-field three-dimensional description of the field except for directions in the plane of the plate where the baffled model is inherently restricted. An improved model, allowing one to evaluate the sound field in all directions from a vibrating body, should be investigated.

The model used for the force (a Hanning window) is another idealization of the reality. This follows from the difficulty in measuring accurately the interaction force between bullet and plate during the impact. However, it has been shown that a good estimation of the impact duration yields satisfactory results even if the exact shape of the force is not known. Measurements of impact forces at low velocity, using a steel tip against a piece of lead, show that the force pulse becomes asymmetric as the deformation becomes plastic. More work is needed here in order to characterize the force pulse at higher velocities.

With the experimental technique, two-dimensional projections of a transient sound field are recorded. For a full three-dimensional description of the field, several projections from a number of directions must be recorded and followed by a tomographic reconstruction. Such reconstructions have been reported for a sound field radiated by an harmonically vibrating surface [13]. In the transient case, reconstructions have been performed for a circular symmetric sound field radiating from an impacted plate [14]. Due to the symmetry, only one projection was needed for the tomographic reconstruction. Reconstructions of a transient, non-circular symmetric sound field have been performed, however, with an electrical discharge as sound source [15]. In this experiment, the sound field diffracted through a double slit (an acoustic Young's experiment) was studied. For a tomographic reconstruction of a transient sound field generated by a plate in the general case, the technique to record the projections needs further development.

ACKNOWLEDGMENT

REFERENCES

1. B. C. MOORE 1982 *An Introduction to the Psychology of Hearing*. London: Academic Press.
2. S. SCHEDIN, A. O. WÅHLIN and P. GREN 1996 *Journal of the Acoustical Society of America* **99**, 700–705. Transient acoustic near field in air generated by impacted plates.
3. S. SCHEDIN, P. GREN and A. O. WÅHLIN 1995 *Proceedings of the* 15*th International Congress on Acoustics ICA'95 Trondheim* **4**, 159–162. Visualization of transient acoustic fields generated by shock loaded plates.
4. S. SCHEDIN, P. GREN and A. O. WÅHLIN 1997 *Shock Waves* **7**, 343–350. Shock waves in an elliptical cavity with varying height.
5. T. KREIS 1996 *Holographic Interferometry, Principles and Methods*. Berlin: Akademie Verlag.
6. A. W. LEISSA 1969 *Vibration of Plates* (NASA-SP-160). Washington, DC: US Government Printing Office.
7. M. C. JUNGER and D. FEIT 1986 *Sound, Structures and their Interaction*. Cambridge, MA: MIT Press; second edition.
8. C. LAMBOURG 1997 *Thèse de doctorat de l'Université du Maine, Le Mans*. Modèle temporel pour la simulation numérique de plaques vibrantes. Application à la synthèse sonore.
9. G. COHEN (editor) 1994 *Méthodes Numériques D'ordre Élevé pour les Ondes en Régime Transitoire*. Rocquencourt: Inria.
10. W. F. AMES 1992 *Numerical Methods for Partial Differential Equations*. San Diego: Academic Press; third edition.
11. A. FRENDI, L. MAESTRELLO and A. BAYLISS 1994 *Journal of Sound and Vibration* **177**, 207–226. Coupling between plate vibration and acoustic radiation.

12. W. GOLDSMITH 1960 *Impact*: *the Theory and Physical Behaviour of Colliding Solids*. London: Edward Arnold.
13. M. ESPELAND, O. LØKBERG and R. RUSTAD 1995 *Journal of the Acoustical Society of America* **98**, 280–287. Full field tomographic reconstruction of sound fields using TV holography.
14. P. GREN and S. SCHEDIN 1998 *Proceedings of the 11th International Conference on Experimental Mechanics*, *Oxford*, 24–28 August, 601–605. Transient wave fields in mechanics and acoustics recorded by pulsed TV holography.
15. P. GREN, S. SCHEDIN and X. LI 1998 *Applied Optics* **37**, 834–840. Tomographic reconstruction of transient acoustic fields recorded by pulsed TV holography.